Monthly Notices of the ROYAL ASTRONOMICAL SOCIETY

MNRAS **488,** 3003–3013 (2019) doi:10.1093/mnras/stz1814
Advance Access publication 2019 July 25

Enhancing AGN efficiency and cool-core formation with anisotropic thermal conduction

David J. Barnes [1]★ Rahul Kannan,[2]† Mark Vogelsberger [1] Christoph Pfrommer,[3] Ewald Puchwein [4,5] Rainer Weinberger,[6] Volker Springel [6,7,8] Rüdiger Pakmor [6] Dylan Nelson,[8] Federico Marinacci [1,2] Annalisa Pillepich,[9] Paul Torrey [1] and Lars Hernquist[2]

[1]*Department of Physics, Kavli Institute for Astrophysics and Space Research, Massachusetts Institute of Technology, Cambridge, MA 02139, USA*
[2]*Harvard–Smithsonian Center for Astrophysics, 60 Garden Street, Cambridge, MA 02138, USA*
[3]*Leibniz-Institut für Astrophysik Potsdam (AIP), An der Sternwarte 16, D-14482 Potsdam, Germany*
[4]*Institute of Astronomy, University of Cambridge, Madingley Road, Cambridge CB3 0HA, UK*
[5]*Kavli Institute for Cosmology, University of Cambridge, Madingley Road, Cambridge CB3 0HA, UK*
[6]*Heidelberg Institute for Theoretical Studies, Schloss-Wolfsbrunnenweg 35, D-69118 Heidelberg, Germany*
[7]*Zentrum für Astronomie der Universität Heidelberg, ARI, Mönchhofstr. 12-14, D-69120 Heidelberg, Germany*
[8]*Max-Planck-Institut für Astrophysik, Karl-Schwarzschild-Str. 1, D-85741 Garching, Germany*
[9]*Max-Planck-Institut für Astronomie, Königstuhl 17, D-69117 Heidelberg, Germany*

Accepted 2019 June 26. Received 2019 May 25; in original form 2018 May 10

ABSTRACT

Understanding how baryonic processes shape the intracluster medium (ICM) is of critical importance to the next generation of galaxy cluster surveys. However, many models of structure formation neglect potentially important physical processes, like anisotropic thermal conduction (ATC). We explore the impact of ATC on the prevalence of cool-cores (CCs) via 12 pairs of magnetohydrodynamical galaxy cluster simulations, using the IllustrisTNG model with and without ATC. Examining their properties we find that the addition of ATC has a negligible impact on the median rotation measure, plasma β, the magnetic field-radial direction angle, and the effective Spitzer value. However, the scatter in the angle and effective Spitzer value is 50 per cent larger with ATC because the magnetic field aligns with the azimuthal direction to a greater extent in relaxed clusters. ATC's impact varies from cluster to cluster and with CC criterion, but its inclusion produces a systematic shift to larger CC fractions at $z = 0$ for all CC criteria considered. Additionally, the inclusion of ATC flattens the CC fraction redshift evolution, helping to ease the tension with the observed evolution. With ATC, the energy required for the central black hole to self-regulate is reduced by 24 per cent and the gas fraction at $0.01\,r_{500}$ increases by 100 per cent, producing larger CC fractions. ATC makes the ICM unstable to perturbations and the increased efficiency of AGN feedback suggests that its inclusion results in a greater level of mixing in the ICM, demonstrated by the 10 per cent reduction in central metallicity for clusters with ATC.

Key words: conduction – methods: numerical – galaxies: clusters: general – galaxies: clusters: intracluster medium.

1 INTRODUCTION

The thermal structure of the hot gas that fills galaxy clusters, the intracluster medium (ICM), is very sensitive to the baryonic processes that are ongoing within the cluster volume. Cooling, heat transport, turbulence, plasma physics, cosmic rays, magnetic fields, and energy injection from supernovae and active galactic nuclei (AGNs) combine to shape the ICM and its observable properties. At the very centre of galaxy clusters, the X-ray emission can become sufficiently intense to imply that the cooling time of the ICM is shorter than the age of the Universe (e.g. Lewis, Stocke & Buote 2002; Peterson et al. 2003). This strong X-ray emission leads to a dense central core with a temperature that is only a third of the

★ E-mail: djbarnes@mit.edu
† Einstein Fellow.

virial temperature of the cluster (e.g. Ikebe et al. 1997; Vikhlinin et al. 2005). This cold, dense thermal structure at the centre of the ICM is known as a cool core (CC) and is associated with a relaxed cluster morphology. Recent observations have shown that CCs exist at high redshift ($z > 1$) and that their properties appear to be roughly independent of redshift (McDonald et al. 2017).

Reproducing the correct fraction of clusters that host a CC in cosmological simulations remains a significant challenge. Even recent numerical work with subgrid prescriptions that include feedback from AGN struggle to reproduce the CC fractions observed in unbiased, low-redshift samples. The exact level of agreement with the observations depends on the chosen CC criteria (e.g. Hudson et al. 2010) and the simulated samples are typically small (∼10–30 objects) due to their computational expense (e.g. Rasia et al. 2015; Hahn et al. 2017). This limits any statistically meaningful comparison between the simulations and the observations. Barnes et al. (2018) recently explored six common CC criteria for galaxy clusters selected from the TNG300 volume of the IllustrisTNG simulations (Marinacci et al. 2018; Naiman et al. 2018; Nelson et al. 2018; Pillepich et al. 2018b; Springel et al. 2018). This provided a sample of 370 clusters at $z = 0$, and they found that the IllustrisTNG model yields reasonable agreement with observed CC fractions at low redshift. However, the evolution of the simulated CC fractions was, in general, found to be 2–3σ steeper than observed.

Due to computational expense, most state-of-the-art cosmological cluster formation simulations include only the minimum physical processes required to reproduce an ICM that has reasonable global properties (e.g. Rasia et al. 2015; Barnes et al. 2017a, b; McCarthy et al. 2017; Henden et al. 2018), i.e. cooling, star formation, and feedback from supernovae and AGN. These simulations neglect a range of physical processes known to be important to the thermal structure of the ICM, like magnetic fields (e.g. Carilli & Taylor 2002), cosmic rays (e.g. Pfrommer 2013; Jacob & Pfrommer 2017a, b; Ruszkowski, Yang & Reynolds 2017; Ehlert et al. 2018), and thermal conduction (e.g. Quataert 2008; Sharma et al. 2009). In a magnetized, hot diffuse plasma, like the ICM, the flow of heat is determined by the temperature gradient and the geometry of the magnetic field, as conduction is strongly suppressed across field lines (Spitzer 1962). The anisotropic flow of heat in the ICM alters its convective stability and leads to the development of the magnetothermal instability (MTI) and the heat-flux-driven buoyancy instability (HBI) (Balbus 2000; Parrish & Stone 2007; Parrish & Quataert 2008; Quataert 2008; Sharma et al. 2009; McCourt et al. 2011). Therefore, anisotropic thermal conduction (ATC) is potentially very important in capturing the thermal structure of the ICM and the presence of a CC (Voigt & Fabian 2004; Voit 2011).

However, the exact impact of ATC in the ICM is still unclear. The strong temperature dependence of the heat flux ($Q \propto T^{7/2}$) requires the conductivity to be fine-tuned to offset radiative losses (Zakamska & Narayan 2003), and solutions are only locally stable on scales of the magnetic field length (Soker 2003). Therefore, thermal conduction likely provides part of the energy required to offset the observed radiative losses (Bogdanović et al. 2009; Sharma et al. 2009; Ruszkowski & Oh 2010; Kunz et al. 2012; Arth et al. 2014; Banerjee & Sharma 2014; Yang & Reynolds 2016), reducing the energy input required from the central AGN. For a single cluster, Kannan et al. (2017) demonstrated that the HBI and MTI triggered by the presence of ATC led to increased mixing in the ICM and a more efficient AGN–ICM coupling. In addition, there is increasing evidence that thermal conduction leads to a bi-modality in the galaxy cluster population (Parrish, Quataert & Sharma 2010; Voit 2011; Arth et al. 2014; Voit & Donahue 2015; Voit et al. 2015; Voit et al. 2017). For clusters whose central cooling time is sufficiently long ($t_{\rm cool} > 1$ Gyr) conduction of heat has been shown to be sufficient to offset radiative losses, but for clusters with short central cooling times ($t_{\rm cool} < 1$ Gyr) the conduction of heat is not sufficient to balance radiative losses and runaway cooling ensues until an AGN feedback event is triggered.

In this paper, we explore the impact of ATC on CC formation and evolution in a set of 12 cosmological galaxy cluster formation simulations. Each cluster is simulated with and without ATC, while the underlying galaxy formation model is kept constant. The vast majority of previous work on the impact of thermal conduction makes use of idealized set-ups, e.g. isolated cubes representing the central core of the ICM, while previous cosmological simulations are missing the required physical processes, e.g. a magnetic field and anisotropic heat transport. Here, we aim to isolate the impact of ATC in a cosmological environment to understand its interplay with AGN feedback and how this impacts the development and maintenance of CCs.

The paper is structured as follows. In Section 2, we provide a brief overview of the clusters in the simulation suite and present our numerical method for anisotropic thermal conduction. We explore the impact of the inclusion of ATC on the cluster properties it is reliant on, i.e. the magnetic field geometry and temperature gradients, in Section 3. The CC criteria used in this work are introduced in Section 4 and we examine how they change with the inclusion of ATC. In Section 5, we explore how changes in the simulated CC fractions link to the efficiency of AGN feedback. Finally, we present our conclusions in Section 6.

2 NUMERICAL METHOD

In this work, we use 12 galaxy clusters from the AESTUS simulation suite. These clusters cover the observed mass range, with 10 covering a narrow mass range $4.20 \times 10^{14}\,{\rm M}_\odot < M_{500}\,/\,{\rm M}_\odot < 8.75 \times 10^{14}\,{\rm M}_\odot$, a poor cluster with a mass $M_{500} = 1.02 \times 10^{14}\,{\rm M}_\odot$ and a rich cluster of mass $M_{500} = 2.72 \times 10^{15}\,{\rm M}_\odot$.[1] The Appendix provides a table of basic cluster properties. The objects were extracted from the Millennium XXL simulation (Angulo et al. 2012), with their cosmological parameters rescaled to the measurements of Planck Collaboration XIII (2016): $\Omega_{\rm M} = 0.3089$, $\Omega_\Lambda = 0.6911$, $\Omega_{\rm b} = 0.0486$, $\sigma_8 = 0.8159$, $n_{\rm s} = 0.9667$, and $H = 100\,h\,{\rm km\,s^{-1}\,Mpc^{-1}}$ with $h = 0.6774$. In the high-resolution region, the dark-matter particles have a mass $m_{\rm DM} = 5.9 \times 10^7\,{\rm M}_\odot$ and the gas cells have a target mass $m_{\rm gas} = 1.1 \times 10^7\,{\rm M}_\odot$. Collisionless particles, i.e. stars and dark matter, have a softening length of 1.48 kpc that is comoving for $z > 1$ and a fixed physical length for $z \leq 1$. The gas cells employ an adaptive co-moving softening length, reaching a minimum of 0.37 kpc. The chosen resolution matches the TNG300 simulation, the largest volume of the IllustrisTNG project.[2]

The simulations employ the IllustrisTNG galaxy formation model (Weinberger et al. 2017; Pillepich et al. 2018a), an updated version of the Illustris model (Vogelsberger et al. 2013; Genel et al. 2014; Torrey et al. 2014; Vogelsberger et al. 2014a, b; Sijacki et al. 2015), that includes radiative cooling, star formation, metal enrichment, magnetic fields, and feedback from supernovae and AGNs. Initial

[1] We define M_{500} as the mass enclosed within a sphere of radius r_{500} whose mean density is 500 times the critical density of the Universe at the cluster's redshift.

[2] http://www.tng-project.org/

results were presented in Springel et al. (2018), Marinacci et al. (2018), Naiman et al. (2018), Nelson et al. (2018), and Pillepich et al. (2018b). The metal distribution in the ICM is well matched to observed clusters (Vogelsberger et al. 2018). A census of the clusters hosting a CC in the TNG300 volume and their evolution with redshift was presented in Barnes et al. (2018). Each cluster in the suite is simulated twice, once with the fiducial TNG model and once with the TNG model that additionally includes ATC.

The numerical implementation of ATC follows the approach introduced in Kannan et al. (2016). The value of the conduction coefficient is set to the canonical Spitzer value (Spitzer 1962) parallel to the magnetic field, with a maximum diffusive value of $\chi = 5 \times 10^{31}\,\mathrm{cm^2\,s^{-1}}$. Thermal conduction relies on the Coulomb collision between particles, and in a magnetized plasma heat transport perpendicular to the magnetic field is strongly suppressed as the Larmor radius of the electron is significantly smaller than its collisional mean free path. For typical ICM conditions ($T = 3\,\mathrm{keV}$, $n_\mathrm{e} = 0.01\,\mathrm{cm^{-3}}$, and $|B| = 1\,\mu\mathrm{G}$), the mean free path is $\lambda_\mathrm{mfp} = 10^{21}\,\mathrm{cm}$ and the Larmor radius is $\lambda_\mathrm{L} = 10^{8}\,\mathrm{cm}$ (Rasera & Chandran 2008; Sharma, Parrish & Quataert 2010; ZuHone et al. 2013; Arth et al. 2014; Dubois & Commerçon 2016). Therefore, we set the conduction coefficient to zero perpendicular to the magnetic field. We note that we neglect the ion component of heat transport, as it is a factor $\sqrt{m_\mathrm{i}/m_\mathrm{e}} \approx 42$ smaller. Our chosen conduction coefficient value is likely optimistic, as plasma effects, like mirror instabilities (Komarov et al. 2016) and Whistler waves (Roberg-Clark et al. 2016), potentially lead to a substantial suppression of thermal conduction. However, we set the coefficient to the canonical Spitzer value to explore the maximum impact on the thermal structure of the ICM. Gaspari & Churazov (2013) have previously argued that the conduction coefficient in the ICM for isotropic conduction is negligible; however, isotropic conduction is incorrect in the presence of a magnetized plasma and the value of the conduction coefficient in the ICM is still unclear. Finally, we note that the conduction routine is not active for star-forming gas cells that follow an imposed equation of state (Springel & Hernquist 2003).

3 CLUSTER PROPERTIES

The anisotropic transport of heat within the ICM depends critically on the temperature gradient and the magnetic field structure. Therefore, we begin our analysis by examining how these properties change with the addition of ATC and how they compare to observed clusters.

The Faraday rotation measure (RM) is a combination of the electron number density and magnetic field along the line of sight, providing information about the strength and coherence length of the magnetic field. RM is defined as

$$\mathrm{RM} = \frac{e^3}{2\pi m_\mathrm{e}^2 c^4} \int_0^L n_\mathrm{e}(l)\, B_\parallel(l)\, \mathrm{d}l, \qquad (1)$$

where e is the electron charge, m_e is the electron mass, c is the speed of light, n_e is the electron number density, and $B_\parallel$ is the component of the magnetic field along the line-of-sight element dl. The RM of each cluster is computed by projecting all particles within a cluster-centric distance of $1.5\,r_{500}$ along the z-direction on to a map with a pixel width 2 kpc. For each pixel in the map, the RM is computed via equation (1). The radial RM profile is then extracted by radially binning the pixels into 50 linearly spaced bins in the radial range of 0–1.75 Mpc. Fig. 1 shows the median absolute RM radial profile for the 12 clusters with (red dashed line) and without (solid blue line) ATC. The shaded and hatched regions show the 5 th and 95 th percentiles. We compare the results to observed RM measurements in galaxy clusters (grey symbols) taken from Kim et al. (1991), Feretti et al. (1999), Clarke et al. (2001), Johnston-Hollitt & Ekers (2004), Govoni et al. (2006), Guidetti et al. (2008), Kuchar & Enßlin (2011), and Böhringer et al. (2016).

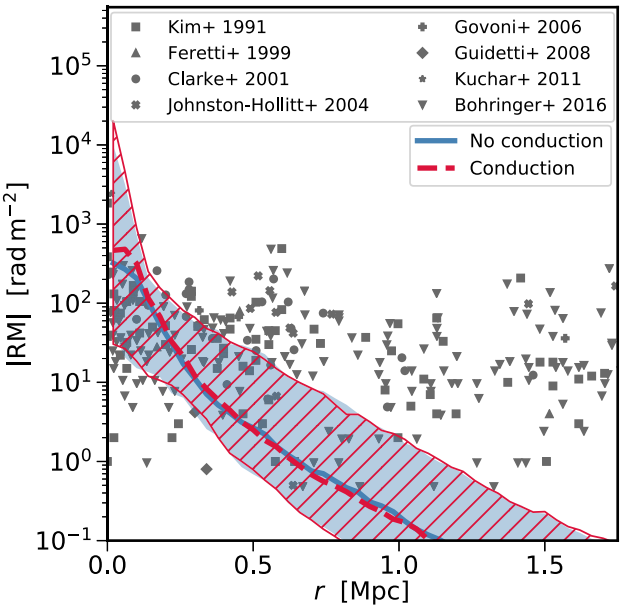

Figure 1. Median absolute Faraday RM radial profile at $z = 0$ without (blue solid line) and with (red dashed line) ATC. The filled blue and the red hatched regions denote the region enclosed by the 5 th and 95 th percentiles without and with ATC, respectively. We compare to observed RM measurements (grey symbols) from Kim, Tribble & Kronberg (1991) (square), Feretti et al. (1999) (upward triangle), Clarke, Kronberg & Böhringer (2001) (circle), Johnston-Hollitt & Ekers (2004) (plus), Govoni et al. (2006) (cross), Guidetti et al. (2008) (diamond), Kuchar & Enßlin (2011) (star), and Böhringer, Chon & Kronberg (2016) (downward triangle). There is a negligible difference between the simulations at all radii. The central simulated median RM measurement is in broad agreement with the observational data; however, it scatters to larger central values and declines more steeply with radial distance than observed.

There is a negligible difference between the median RM radial profile, and the 5 th and 95 th percentiles of clusters simulated with ATC and those simulated without it. Both cluster samples reach an absolute central RM value of $\sim 3 \times 10^2\,\mathrm{rad\,m^{-2}}$ and this value declines steeply with radius. Regardless of the inclusion of ATC, we see the spread in the profiles increasing with radial distance. The absolute central median value and radial decline of the RM profile are in broad agreement with the much larger sample of clusters from the TNG300 level-1 volume (Marinacci et al. 2018). The central median RM magnitudes are in broad agreement with the observational data, sitting at the top of the observational scatter. However, the scatter in simulated values reaches a maximum of $\times 10^4\,\mathrm{rad\,m^{-2}}$, which is a factor of $\sim$4 larger than the most extreme observed value. In addition, the decline with radial distance is steeper than observed. We note that we do not account for observational effects such as Faraday depolarization.

The difference between the simulated and observed samples may be due to the decreasing numerical resolution of the simulations with radial distance, which is a consequence of the chosen refinement scheme and the pseudo-Lagrangian nature of the AREPO code that results in the resolution being density dependent (Nelson et al.

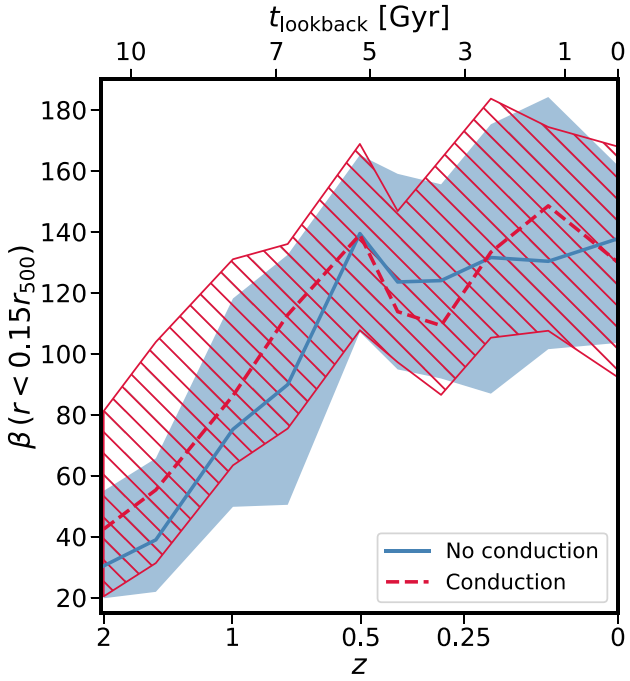

Figure 2. Median plasma beta, $\beta \equiv P_{\rm th}/P_{\rm mag}$, averaged within $0.15\,r_{500}$ as a function of redshift for simulations without (blue solid) and with ATC (red dashed). The blue solid region and the red hatched regions denote the 1σ scatter without and with ATC, respectively. As the clusters form from $z = 2$ to $z = 0.5$, the thermal energy increases more rapidly than the magnetic energy, resulting in an increase in average β value. From $z = 0.5$ to $z = 0$, the β value is constant. The addition of ATC yields little difference in the β value.

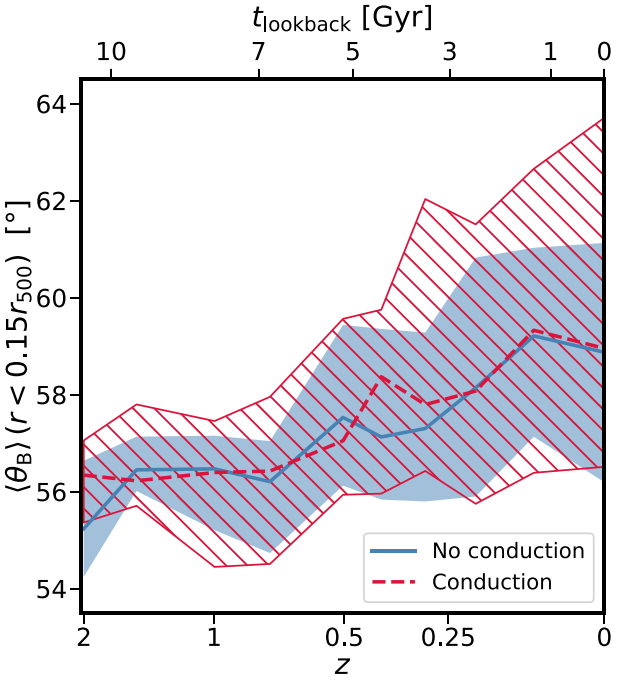

Figure 3. Median angle between the magnetic field and the cluster-centric radial direction averaged with $0.15\,r_{500}$ as a function of redshift for simulations without and with ATC. Line styles are the same as Fig. 2. The median angle between the magnetic field and the radial direction is roughly constant with redshift, suggesting turbulent random re-orientation dominates over HBI azimuthal re-orientation. The scatter in the angle increases by 50 per cent with ATC, suggesting it is more important in more relaxed clusters.

2016). It had been argued that the lack of ATC in the IllustrisTNG simulations was a potential cause of the steeper than observed declines; however, we rule that out. A final possibility is that the simulations are not capturing the increased amplification of the magnetic field with cluster-centric radial distance due to the increasing level of turbulent motions, a result of radially declining numerical resolution. However, this would require detailed higher resolution simulations to explore this effect (e.g. Vazza et al. 2018).

The impact of ATC is dependent on the plasma beta $\beta \equiv P_{\rm th}/P_{\rm mag}$, the ratio of the thermal pressure to the magnetic pressure. For realistic β values within the ICM the saturation properties of HBI differ from the idealized, large or infinite β value simulations (Avara, Reynolds & Bogdanović 2013). In Fig. 2, we plot the median β value within $0.15\,r_{500}$ as a function of redshift for simulations with and without ATC. As the clusters collapse and form between $z = 2$ and $z = 0.5$, we find that the plasmaβ linearly increases from a value of $\beta \approx 30$–40 to $\beta \approx 130$. Therefore, the magnetic field is amplified during the initial collapse of the cluster progenitors and the thermal energy increases as the progenitors merge to form the ICM (Marinacci et al. 2015). Once the ICM has formed the β value remains constant. The evolution of the plasma β with redshift is independent of the inclusion of ATC, with its normalization and scatter consistent between simulations with and without it. There is some suggestion that the plasma β is larger at high redshift ($z > 0.75$) with ATC, but they are still consistent within the 1σ scatter.

In Fig. 3, we plot the median average alignment of the magnetic field with the cluster-centric radial direction, where $\theta_{\rm B} \equiv \arccos|\hat{b} \cdot \hat{r}|$, within $0.15r_{500}$ as a function of redshift for simulated clusters with and without ATC. Regardless of the inclusion of ATC, we find that the average angle between the radial direction and the magnetic field marginally increases between $z = 2$ and $z = 0$, increasing by $\sim 3^\circ$ over 10 Gyr. This is potentially driven by the evolution of the halo accretion rate. When ATC is included, the angle of the magnetic field is a competition between the HBI and turbulent motions. Turbulence will randomly orientate the magnetic field and the HBI re-orientates the magnetic field in the azimuthal direction, which occurs more rapidly in higher β plasmas (Avara et al. 2013). The lack of difference in the magnetic field angle relative to the radial direction between those clusters with ATC and without suggests that turbulent re-orientation dominates HBI alignment in a realistic cosmological setting. The median value is consistent with the 57.3° expected for an isotropic distribution.

The angle between the magnetic field and the radial direction is important because it determines the amount of heat that can be transported into the cluster core. The average angle corresponds to an effective Spitzer fraction, $f_{\rm eff} \approx (\hat{b} \cdot \hat{r})^2 = \cos^2\theta_{\rm B}$. In Fig. 4, we plot the median effective Spitzer fraction averaged within $0.15\,r_{500}$ as a function of redshift for the cluster sample with and without ATC. Although anisotropic heat flow will not occur in the simulations without ATC, they provide a baseline to compare how the differences induced in the magnetic field by ATC impact the heat transport properties. The effective Spitzer fraction is approximately constant with redshift, decreasing mildly from 0.35 at $z = 2$ to 0.31 at $z = 0$. The scatter in effective Spitzer fractions for the cluster sample simulated with ATC reaches smaller values relative to clusters without ATC. The magnetic field angle and effective Spitzer coefficients are consistent with previous work in more idealized set-ups (e.g. Yang & Reynolds 2016).

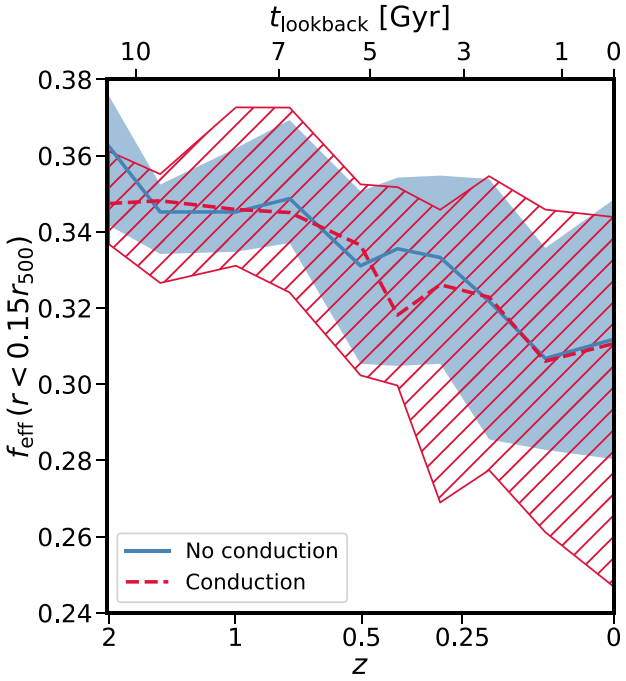

Figure 4. Median effective Spitzer fraction averaged within $0.15\,r_{500}$ as a function of redshift for the cluster sample with and without ATC. Line styles are the same as Fig. 2. The effective Spitzer fraction decreases mildly with redshift. The increased impact of ATC in relaxed clusters leads to further suppression of the effective Spitzer coefficient.

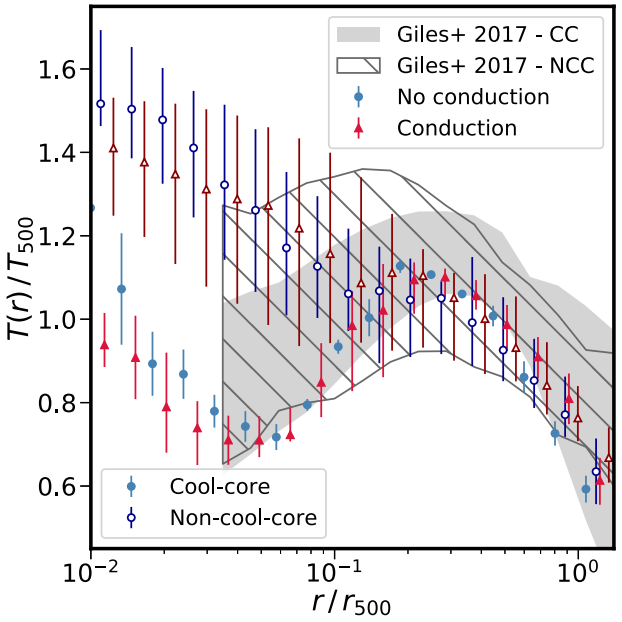

Figure 5. Median spectroscopic radial temperature profiles for simulations with (red triangles) and without (blue circles) ATC at $z = 0$. We compare to the observed cluster sample from Giles et al. (2017) (grey band). For both simulations and observations, the clusters are divided into CC (filled) or NCC (open) samples via the central density cuspiness criterion, with a threshold $\alpha > 0.7$ defining a CC. We note we have offset the points marginally for clarity. The simulations are good agreement with the observed profiles.

Besides the magnetic field, the other component required for anisotropic heat flow is a rising temperature gradient with increasing cluster-centric radial distance. In Fig. 5, we plot the median spectroscopic radial temperature profiles simulated with and without ATC as a function of r_{500} at $z = 0$. We compare to the observational sample of Giles et al. (2017), as the median mass of the sample is well matched to the median mass of the simulated clusters. All samples are split into CC and NCC clusters via the cuspiness of the gas density profile α, classifying a cluster as CC if $\alpha > 0.7$ and as a NCC otherwise. As more massive clusters have deeper potential wells, and as a consequence higher temperatures, we divide each profile by the expected virial temperature of the system to remove the mass dependence. This is defined as

$$k_{\rm B} T_{500} = \frac{G M_{500}\, \mu m_{\rm p}}{2 r_{500}}, \tag{2}$$

where G is the gravitational constant, $\mu = 0.59$ is the mean molecular weight, and $m_{\rm p}$ is the proton mass. Beyond approximately $0.3\,r_{500}$, we find that both CC and NCC clusters have similar profiles, regardless of the inclusion of ATC, and that they are in good agreement with the observational data. The NCC profiles continue to increase in temperature within $0.3\,r_{500}$ and are well matched to the observed NCC profile. The CC profiles turnover inside 0.15–$0.2\,r_{500}$, reducing in temperature by 35 per cent relative to the peak temperature at $0.2\,r_{500}$. The CC profiles then increase in temperature for $r < 0.05 r_{500}$, likely due to AGN feedback. When split into CC and NCC samples, we find that the addition of ATC to galaxy formation model has negligible impact on the median temperature profiles, being consistent with each other at all radii for both samples.

In general, we find that the magnetic field geometry of simulated clusters is in broad agreement with observed clusters, but the amplitude of the magnetic field is potentially slightly too large in the very centre of the simulated clusters. The median plasma β, magnetic field alignment, and effective Spitzer fraction are consistent with and without ATC as a function of redshift. However, the scatter in the magnetic field alignment and effective Spitzer fraction are larger when ATC is included. The temperature profiles of the clusters are in good agreement with the observed temperature profiles. We now examine how ATC impacts the fraction of clusters that host a CC.

4 CC FRACTIONS AND REDSHIFT EVOLUTION

The literature contains many ways of defining a CC cluster and the fraction of clusters defined as CC depends on the chosen criterion and the sample selection. Observationally, the chosen criterion can depend on the quality and resolution of the data, for example whether the data are of sufficient quality to allow a reliable temperature profile to be extracted. We use the same six criteria as Barnes et al. (2018), examining CC defined by the central electron number density, the central cooling time, the central entropy excess, the concentration parameter measured within scaled and physical apertures, and the cuspiness parameter. The notation, CC threshold, and measurement aperture for each criterion are summarized in Table 1. We refer the interested reader to Barnes et al. (2018) for a thorough description of each criterion and the observational references from which the thresholds are taken.

In the main panels of Fig. 6, we present the CC criteria as a function of M_{500} at $z = 0$ for the simulated clusters with and without ATC. The impact of ATC varies for matched pairs of clusters, with several clusters showing a large shift towards the CC tail of the criterion distribution and two clusters producing small shifts

Table 1. Table summarizing the CC criteria used in this work. The columns denote the CC criterion, the notation used throughout this work, the aperture within which the criterion is measured, the threshold used to define a CC, and the number of clusters defined as a CC at $z = 0$ with and without ATC.

Criterion	Notation	Aperture	CC limit	Number of CC clusters	
				With ATC	Without ATC
Central electron number density	n_e	$0.012\,r_{500}$	$> 1.5 \times 10^{-2}$ cm^{-3}	8	6
Central cooling time	t_{cool}	$0.012\,r_{500}$	< 1 Gyr	5	3
Central entropy excess	K_0	–	< 30 keV cm^{-2}	4	2
Concentration parameter (physical)	C_{phys}	40.0, 400.0 kpc	>0.155	5	3
Concentration parameter (scaled)	C_{scal}	0.15, $1.0\,r_{500}$	>0.5	7	6
Cuspiness parameter	α	$0.04\,r_{500}$	>0.75	4	2

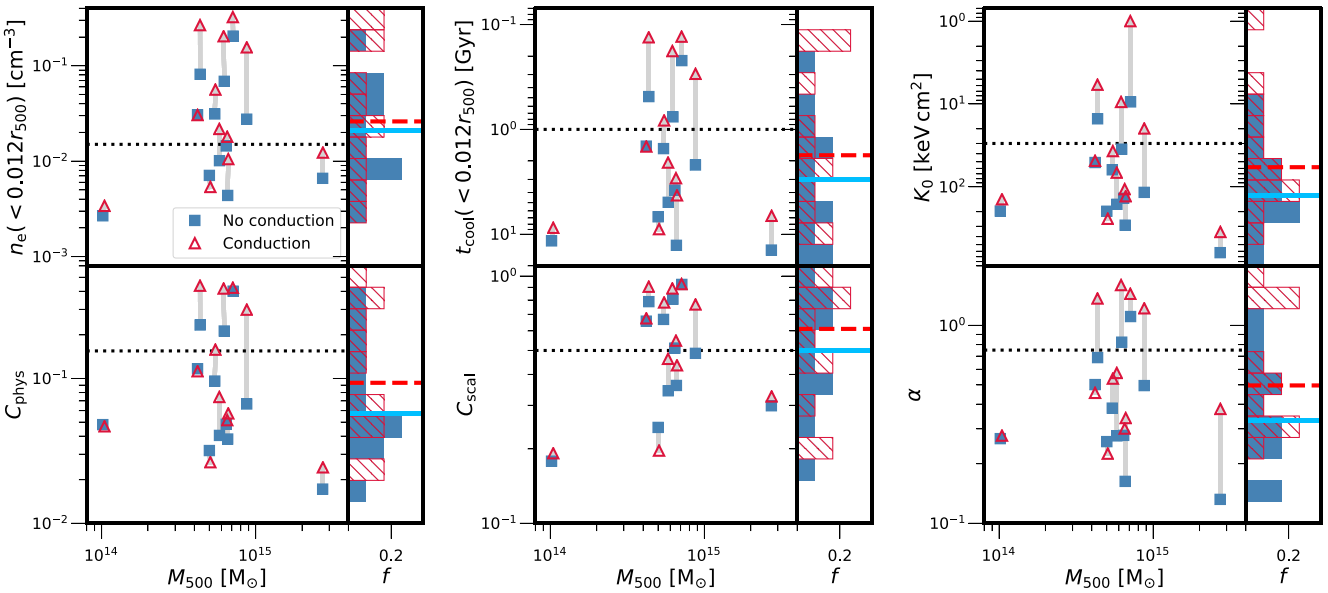

Figure 6. Six different CC criteria at $z = 0$ for the clusters run with (red triangle) and without (blue square) anisotropic thermal conduction. Grey lines link matched clusters with the dotted black line denoting the CC threshold. We note the y-axis is inverted for the cooling time and central entropy excess. In the side panels, the criteria distributions with (red hashed) and without (solid blue) are shown, with the median of the distributions denoted by the red dashed and blue solid lines, respectively. The inclusion of anisotropic thermal conduction produces a systematic shift towards larger CC fractions.

towards the non-cool-core (NCC) tail. The change induced on a cluster pair by ATC also varies from criterion to criterion. This result is not unexpected, previous observational work has shown the correlation between CC criteria is not perfect (Andrade-Santos et al. 2017) and CC thresholds are observationally defined, rather than originating from a systematic numerical study that ensures they select the same objects.

The side of each CC criterion panel shows the distribution of the 12 clusters with and without ATC, with the median value of the distributions shown by the solid and dashed lines, respectively. For all criteria examined in this work, we see a systematic shift of the distribution towards a larger fraction of objects hosting a CC when ATC is included. The fractional changes in the median CC criteria values relative to simulations with ATC are $\Delta n_e/n_e = 0.28$, $\Delta t_{cool}/t_{cool} = -0.43$, $\Delta K_0/K_0 = -0.50$, $\Delta C_{phys}/C_{phys} = 0.62$, $\Delta C_{scal}/C_{scal} = 0.22$, $\Delta\alpha/\alpha = 0.51$.

To explore the shift to larger CC fractions with the inclusion of ATC, we plot the mean cumulative gas fraction radial profiles at $z = 0$ for the simulated cluster with and without ATC in Fig. 7. Barnes et al. (2018) demonstrated that the shape of the gas fraction profile for IllustrisTNG model is inconsistent with the observed profile (Pratt et al. 2010), even when the samples are matched in median mass. This discrepancy is driven by two effects. First, the AGN feedback at high redshift is not efficient enough at ejecting gas from the progenitor haloes of the clusters, which results in the clusters being too gas rich. Secondly, the AGN feedback at late times is too violent and injects too much thermal energy in the cluster core, reducing the central gas fraction below observations and increasing the central temperature above the observations. The addition of ATC has minimal impact on the high-redshift efficiency, as the total gas fraction within r_{500} changes by 1 per cent. To reduce the total gas content within the cluster requires a model of AGN feedback that is more efficient at ejecting material from haloes at high redshift.

However, the distribution of the gas within the cluster has changed significantly. The central gas fraction at $0.01r_{500}$ increases by 100 per cent with ATC, which suggests the energy injected by the central AGN has decreased. In addition, about a third of systems see the cumulative gas fraction exceed the universal baryon fraction (Ω_b/Ω_M) between 0.07 and $0.2\,r_{500}$. This suggests that a greater fraction of the AGN feedback is confined to cluster core when ATC is included, leading to cooling gas external to the core to building up at $\sim 0.15\,r_{500}$. We note that all of the clusters whose gas profiles exceed the universal fraction are defined as CCs via the central electron number density measured at 0.012, r_{500}. In contrast, the

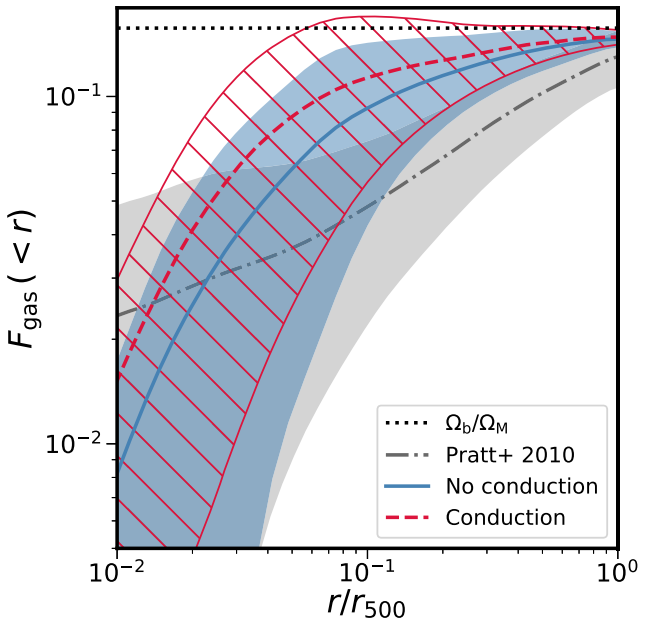

Figure 7. Cumulative mean gas fraction profile at $z = 0$ with (red dashed) and without (blue solid) ATC. The shaded region denotes one standard deviation of the sample. The mean observed gas fraction profile (grey dash–dotted) and associated standard deviation are from the REXCESS cluster sample (Pratt et al. 2010). The inclusion leads to an increased gas fraction throughout the cluster volume, but especially in the cores of clusters defined as CC.

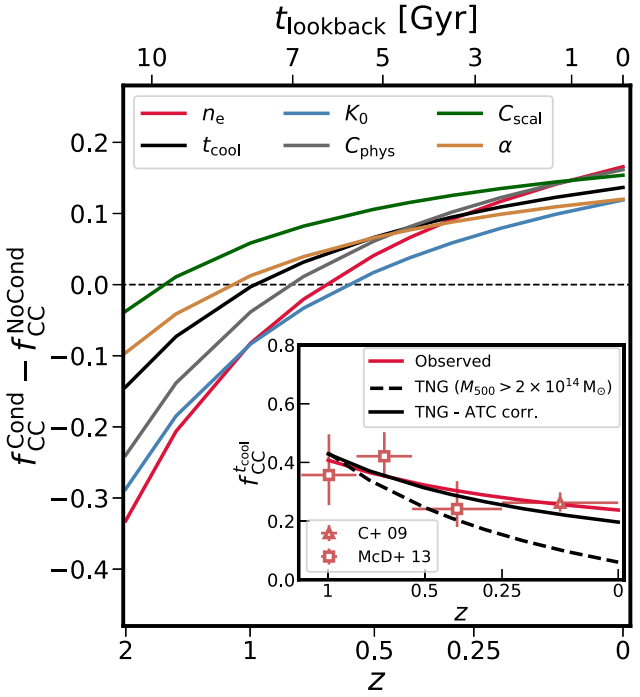

Figure 8. CC fraction difference with and without ATC as a function of redshift, for the central electron number density (red), cooling time (black), central entropy excess (blue), physical (grey) and scaled (green) concentration parameters, and the cuspiness parameter (yellow). *Inset*: Defining CCs by the central cooling time criterion, the correction factor eases the tension with the observed evolution (Cavagnolo et al. 2009; McDonald et al. 2013) for the IllustrisTNG high-mass sample (Barnes et al. 2018).

cumulative gas fraction profiles of NCC systems remain relatively unchanged with the inclusion of ATC. If the high-redshift AGN reduced the total gas content of the clusters, ATC will still have the same effect as long as it did not lead to a significant change in the magnetic field geometry or temperature gradients. However, as both of these are well matched to observations, ideally any meaningful change would have to continue to reproduce these two aspects of the ICM as well as reduce the gas fraction.

With ATC, the gas fractions are systematically higher at $0.012r_{500}$, which will shift the central electron number density to higher values and result in a greater fraction of CCs for a fixed density threshold. With $t_{\rm cool} \propto n_{\rm e}^{-1}$ and $K \propto n_{\rm e}^{-2/3}$, the increased central density will result in a shorter cooling time and a lower central entropy excess, again resulting in higher CC fractions. Finally, higher central densities will increase the X-ray emission from cluster cores, due to its $n_{\rm e}^2$ dependence, and result in larger concentration parameter values and more clusters being defined as CCs. This suggests that the energy injected by the central AGN has reduced, leading to higher central gas fractions and more cluster being classified as CCs.

Since the CC fraction for all six criteria increased at $z = 0$ with the introduction of ATC, we now explore its impact on the CC fraction as a function of redshift. For all six criteria, we calculate the CC fraction between $z = 2$ and $z = 0$, estimating the 1σ confidence intervals via the β distribution quantile technique (Cameron 2011), and then estimate the redshift evolution by fitting a linear relation that accounts for the uncertainties in CC fraction (e.g. Barnes et al. 2018). We perform this fit for both samples, with and without ATC, and the difference between them is shown in the main panel of Fig. 8. The addition of ATC yields the same trend for all six criteria, a reduction in the CC fraction at high redshift ($z > 1$) and an increase in the CC fraction at low redshift. The exact change is dependent on the selected criterion, with the scaled concentration parameter showing the smallest reduction at $z = 2$ ($\Delta f_{\rm CC} = -0.06$) and one of the largest increases in CC fraction at $z = 0$ ($\Delta f_{\rm CC} = 0.17$). The central entropy excess has the shallowest change between $z = 2$ and $z = 0$ and the smallest increase in the CC fraction at low redshift. Barnes et al. (2018) demonstrated that in general the IllustrisTNG model underproduced CCs at low-redshift and overproduced them at high-redshift. In the inset of Fig. 8, we demonstrate that applying the correction factor to the redshift evolution found for such a statistically large sample, specifically the high-mass ($M_{500} > 2 \times 10^{14}\,{\rm M}_\odot$) IllustrisTNG sample, eases tension with the observed redshift evolution trend for the central cooling time criterion. The observations are taken from Cavagnolo et al. (2009, C+ 09) and McDonald et al. (2013, McD+ 13). For all criteria, the addition of ATC would ease the tension with the observed redshift evolution, even if the normalization of the CC fraction still differs from observations.

5 THE LINK TO AGN EFFICIENCY

The inclusion of ATC leads to an increased CC fraction, increased central cumulative gas fraction, and flattens the CC fraction redshift evolution relative to simulations that neglect it. The temperature profiles and the gas fraction profiles both suggest that the central black hole injects less energy into the ICM when thermal conduction is included. Therefore, we now examine the energy injected by the central black hole and how this energy couples to the ICM. We define the central black hole of each cluster as the most massive black hole within 1 kpc of the potential minimum at $z = 0$. Its properties are then traced as a function of redshift. During the

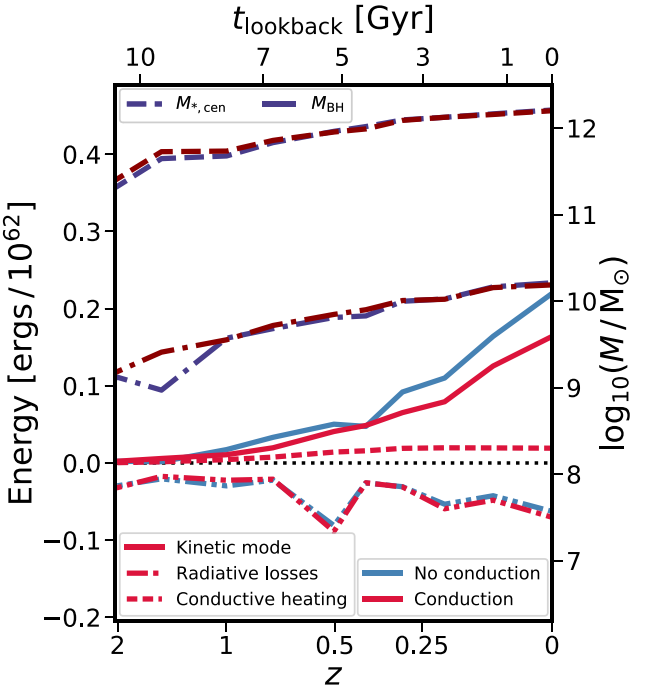

Figure 9. Median cumulative energy injected in the kinetic mode (solid lines) as a function of redshift for the central black hole compared to the energy lost via radiative cooling within r_{500} (dash–dot-dotted lines) for simulations with (red) and without (blue). For simulations with ATC, we plot the conductive heating (short dashed line) within $0.15\,r_{500}$ as a function of redshift. The right scale shows the median stellar mass (long-dashed) and black hole mass (dash-dotted) with (dark red) and without (dark blue) ATC. When ATC is included the central black hole injects less energy, but the stellar and black hole masses are unchanged. Conductive heating only contributes a small fraction of the energy difference.

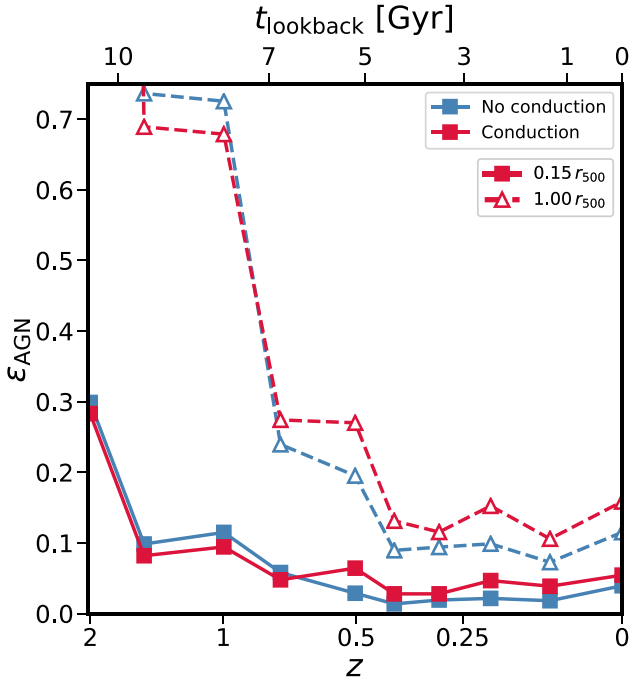

Figure 10. Median AGN efficiency as a function of redshift for simulations with(red) and without (blue) ATC. The efficiency is defined as the total cumulative energy lost via radiative cooling over the cumulative energy injected by the central AGN. The energy lost is measured within $0.15\,r_{500}$ (dashed) and r_{500} (solid). Simulations with ATC have a more efficient AGN feedback at low redshift ($z < 1$).

formation of the ICM ($z \leq 2$) the low accretion rate, kinetic mode feedback dominates (Weinberger et al. 2018). In Fig. 9, we plot the median cumulative energy injected by the central black hole in the kinetic mode feedback for simulations with and without ATC. At $z = 0$, the inclusion of ATC results in a 24 per cent reduction in the energy injected by the low accretion rate kinetic feedback mode, which agrees with the results from the temperature and gas fraction plots.

The right axis of Fig. 9 shows the median stellar mass of the brightest cluster galaxy, defined as the mass within twice the stellar half-mass radius for the most massive subhalo, and the median central black hole mass as a function of redshift. Despite the reduction in energy produced by the inclusion of ATC, the masses of the galaxy and black hole have a negligible difference for simulations with and without ATC, especially for $z \leq 1$. Therefore, the central black hole is still able to self-regulate and control its growth and the growth of the galaxy.

One explanation of the difference in injected energy with and without ATC is that there is significant heat transfer from outer radii into the core of the cluster, providing the additional energy required to offset radiative losses. To investigate this we define the conductive heating with a sphere by its conductive luminosity. This is defined as the heat flux integrated over the surface of the sphere

$$L_{\rm cond} = -f_{\rm eff}\,\chi\,\partial T\,/\,\partial r, \tag{3}$$

where we chose a sphere of radius $0.15\,r_{500}$ to account for the collapse and growth of the cluster with cosmic time. Only gas that is non-star-forming, cooling and has a temperature $T \geq 10^6$ K is included in the conductive luminosity calculation. The red dashed line in Fig. 9 shows the medium cumulative conduction luminosity as a function of redshift for the simulations with ATC. The conductive luminosity is significantly smaller than the energy injected by the central AGN. At $z = 0$, the cumulative conductive luminosity is 1.92×10^{61} erg, which only accounts for 34 per cent of the energy difference between simulations with and without ATC. Therefore, we conclude that ATC is capable of helping to offset radiative losses, but it does not explain the majority of the difference between simulations with and without ATC.

The lack of change in stellar and black hole mass for the central galaxies indicates that the AGN is still self-regulating in the simulations with ATC, despite the central AGN injecting less energy. In Fig. 9, we plot the radiative losses within r_{500} (dash–dot-dotted) as a function of redshift. We only consider non-star-forming gas that is cooling, i.e. not being heated by supernovae or AGN feedback, and has a temperature $T \geq 10^6$ K. The difference in radiative losses between simulations with and without ATC is negligible. Therefore, this suggests that AGN feedback is coupling energy more efficiently to the ICM when ATC is included.

We define AGN efficiency, ε, as the ratio of the total cumulative energy lost by the ICM via radiative cooling over the cumulative energy injected by the central AGN. Fig. 10 shows the median AGN efficiency with and without ATC as a function of redshift, measured inside spherical apertures of $0.15\,r_{500}$ and r_{500}. Regardless of the inclusion ATC, AGN efficiency decreases towards low redshift, reducing by a factor of $\sim$5 between $z = 2$ and $z = 0$ for both apertures. The increased efficiency at high redshift is a combination of the AGN injecting less energy and the increasing critical density of the Universe with redshift, which results in shorter gas cooling

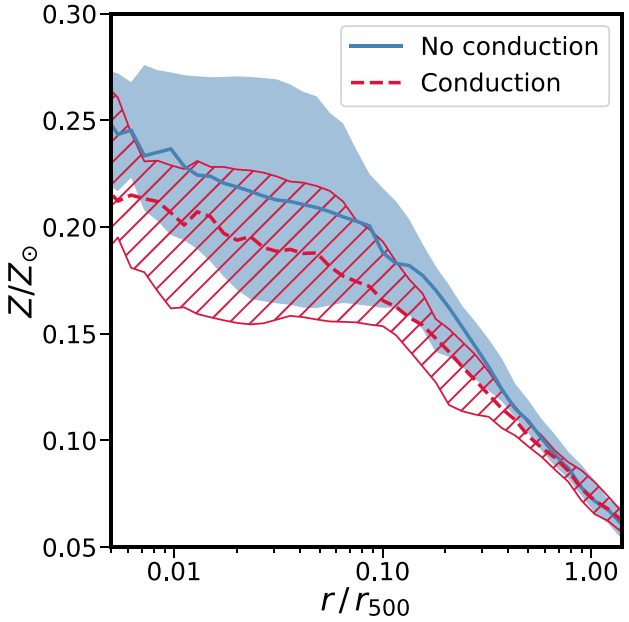

Figure 11. Median radial metallicity profile at $z = 0$ for simulations with and without ATC. Line styles are the same as Fig. 2. When ATC is included, we see a reduction the central metallicity of the cluster, suggestive that more mixing occurs in cluster cores.

times (due to its $1/n$ dependence) and greater energy loss. At low redshift ($z < 1$), the inclusion of ATC yields more efficient AGN feedback.

The introduction of ATC fundamentally changes the response of the ICM to perturbations, such as AGN feedback. In the presence of a temperature gradient, it is unstable to both the HBI (e.g. Quataert 2008) and the MTI (Balbus 2000) and perturbations result in plasma mixing (e.g. Sharma et al. 2009). Using the Monte Carlo tracer particles (Genel et al. 2013) to track gas motions, Kannan et al. (2017) demonstrated that, for a single cluster, the inclusion of ATC lead to a greater level of mixing. A consequence of this increased level of mixing was a reduction in the metallicity of the gas in the cluster core. A key result of this study is that we find the energy injection required by the central AGN to offset radiative losses is reduced when ATC is included. This softens the impact of the central AGN and increases the central gas density, shifting the CC criteria distributions towards a greater fraction of CCs. The increased coupling efficiency when ATC is included suggests a greater level of mixing in the ICM, which would distribute the kinetic mode feedback more isotropically. Lacking the tracer particles in this study, we instead examine the median radial metallicity profile $z = 0$ for clusters simulated with and without ATC in Fig. 11. Abundances have been normalized to Anders & Grevesse (1989). Similar to Kannan et al. (2017), we find that when ATC is included the median metallicity is reduced by 12 per cent at $0.1\,r_{500}$ relative to the simulations without ATC. This suggests that the cluster cores experience a greater level of mixing when ATC is included.

6 CONCLUSIONS

We have examined the impact of ATC on CC formation and the efficiency of AGN feedback using 12 zoom cosmological MHD galaxy cluster simulations. Each cluster was run using the IllustrisTNG galaxy formation model. For one set of runs, we self-consistently included ATC following the method of Kannan et al. (2016). Our main results are as follows:

(i) Examining the rotation measure radial profiles, we find that the simulated clusters are broadly in agreement with the observations, but the central magnetic field amplitude is potentially too large and the radial decline is steeper than observed. This agrees with previous numerical work of Marinacci et al. (2018).

(ii) The median β ratio (Fig. 2), magnetic field angle (Fig. 3), the effective Spitzer value (Fig. 4), and redshift evolution are independent of ATC. However, the inclusion of ATC leads to a greater scatter in the alignment between the magnetic field and the radial direction and the effective Spitzer value.

(iii) The median spectroscopic temperature profiles for CC and NCC clusters are in good agreement with observed clusters (Fig. 5). Outside the core ($r > 0.2\,r_{500}$), all profiles are consistent with each other. Inside the core, NCC clusters continue to increase in temperature, while CC clusters reduce in temperature by 35 per cent from the peak. When already split into CC and NCC clusters, we find that ATC has a negligible impact.

(iv) The impact of ATC on CC criteria varies on a cluster by cluster and criterion-by-criterion basis, but its inclusion produces a systematic shift of all criteria to larger CC fractions (Fig. 6). This change is driven by the increased central gas fraction in the cores of clusters with ATC (Fig. 7).

(v) Exploring the redshift evolution of the CC fraction, the inclusion of ATC results in a decreased CC fraction at high redshift ($z \geq 1$) and an increased CC fraction at low redshift ($z < 1$) (Fig. 8). For the statistically large sample produced by IllustrisTNG (Barnes et al. 2018), the correction due to ATC eases the tension between the simulated and observed redshift evolution of the CC fraction.

(vi) Examining the total energy injected by the central black hole demonstrates that the inclusion of ATC results in the low accretion rate, kinetic mode feedback injecting 24 per cent less energy during the formation of the cluster (Fig. 9). However, the median stellar mass and black hole mass of the central galaxies are unchanged. The transport of heat from larger radii accounts for 34 per cent of the energy difference between simulations with and without ATC. The increased AGN efficiency (Fig. 10) suggests that ATC increases the mixing in the ICM, increasing the efficiency of the AGN feedback–ICM coupling and reducing the energy required for self-regulation. The reduction in the central median metallicity radial profile at $z = 0$ for simulations with ATC relative to simulations without (Fig. 11) provides further evidence of increasing mixing in the ICM of clusters with ATC.

The results suggest that the inclusion of ATC alters the response of the ICM to AGN feedback, making it unstable to convective mixing in the presence of external perturbations. The increased mixing makes the AGN–ICM coupling more efficient, reducing the energy required for self-regulation (e.g. Kannan et al. 2017). This results in increased low-redshift CC fractions and a flatter redshift evolution compared to the same model without ATC. Previous numerical work with artificial thermal conduction that promoted mixing also found an improved match to observed CC fractions (Rasia et al. 2015). The inclusion of ATC reduces the energy injected by a self-regulating black hole, highlighting that it is physical process that potentially impacts the central thermal structure of galaxy clusters.

ACKNOWLEDGEMENTS

The simulations were performed on the MKI-Harvard Odyssey cluster and the Stampede supercomputers at the Texas Advanced

Computing Center as part of XSEDE project TG-AST160069. RK acknowledges support from NASA through Einstein Postdoctoral Fellowship grant number PF7-180163 awarded by the *Chandra* X-ray Center, which is operated by the Smithsonian Astrophysical Observatory for NASA under contract NAS8-03060. MV acknowledges support through an MIT RSC award, the support of the Alfred P. Sloan Foundation, and support by NASA ATP grant NNX17AG29G. PT acknowledges support from NASA through Hubble Fellowship grants HST-HF2-51384.001-A awarded by the STScI, which is operated by the Association of Universities for Research in Astronomy, Inc., for NASA, under contract NAS5-26555. CP acknowledges support by the European Research Council under ERC-CoG grant CRAGSMAN-646955.

REFERENCES

Anders E., Grevesse N., 1989, Geochim. Cosmochim. Acta, 53, 197
Andrade-Santos F. et al., 2017, ApJ, 843, 76
Angulo R. E., Springel V., White S. D. M., Jenkins A., Baugh C. M., Frenk C. S., 2012, MNRAS, 426, 2046
Arth A., Dolag K., Beck A. M., Petkova M., Lesch H., 2014, preprint(arXiv: 1412.6533)
Avara M. J., Reynolds C. S., Bogdanović T., 2013, ApJ, 773, 171
Balbus S. A., 2000, ApJ, 534, 420
Banerjee N., Sharma P., 2014, MNRAS, 443, 687
Barnes D. J. et al., 2017b, MNRAS, 471, 1088
Barnes D. J. et al., 2018, MNRAS, 481, 1809
Barnes D. J., Kay S. T., Henson M. A., McCarthy I. G., Schaye J., Jenkins A., 2017a, MNRAS, 465, 213
Bogdanović T., Reynolds C. S., Balbus S. A., Parrish I. J., 2009, ApJ, 704, 211
Böhringer H., Chon G., Kronberg P. P., 2016, A&A, 596, A22
Cameron E., 2011, PASA, 28, 128
Carilli C. L., Taylor G. B., 2002, ARA&A, 40, 319
Cavagnolo K. W., Donahue M., Voit G. M., Sun M., 2009, ApJS, 182, 12
Clarke T. E., Kronberg P. P., Böhringer H., 2001, ApJ, 547, L111
Dubois Y., Commerçon B., 2016, A&A, 585, A138
Ehlert K., Weinberger R., Pfrommer C., Pakmor R., Springel V., 2018, MNRAS, 481, 2878
Feretti L., Dallacasa D., Govoni F., Giovannini G., Taylor G. B., Klein U., 1999, A&A, 344, 472
Gaspari M., Churazov E., 2013, A&A, 559, A78
Genel S. et al., 2014, MNRAS, 445, 175
Genel S., Vogelsberger M., Nelson D., Sijacki D., Springel V., Hernquist L., 2013, MNRAS, 435, 1426
Giles P. A. et al., 2017, MNRAS, 465, 858
Govoni F., Murgia M., Feretti L., Giovannini G., Dolag K., Taylor G. B., 2006, A&A, 460, 425
Guidetti D., Murgia M., Govoni F., Parma P., Gregorini L., de Ruiter H. R., Cameron R. A., Fanti R., 2008, A&A, 483, 699
Hahn O., Martizzi D., Wu H.-Y., Evrard A. E., Teyssier R., Wechsler R. H., 2017, MNRAS, 470, 166
Henden N. A., Puchwein E., Shen S., Sijacki D., 2018, MNRAS, 479, 5385
Hudson D. S., Mittal R., Reiprich T. H., Nulsen P. E. J., Andernach H., Sarazin C. L., 2010, A&A, 513, A37
Ikebe Y. et al., 1997, ApJ, 481, 660
Jacob S., Pfrommer C., 2017a, MNRAS, 467, 1449
Jacob S., Pfrommer C., 2017b, MNRAS, 467, 1478
Johnston-Hollitt M., Ekers R. D., 2004, arXiv Astrophysics e-prints
Kannan R., Springel V., Pakmor R., Marinacci F., Vogelsberger M., 2016, MNRAS, 458, 410
Kannan R., Vogelsberger M., Pfrommer C., Weinberger R., Springel V., Hernquist L., Puchwein E., Pakmor R., 2017, ApJ, 837, L18
Kim K.-T., Tribble P. C., Kronberg P. P., 1991, ApJ, 379, 80
Komarov S. V., Churazov E. M., Kunz M. W., Schekochihin A. A., 2016, MNRAS, 460, 467
Kuchar P., Enßlin T. A., 2011, A&A, 529, A13
Kunz M. W., Bogdanović T., Reynolds C. S., Stone J. M., 2012, ApJ, 754, 122
Lewis A. D., Stocke J. T., Buote D. A., 2002, ApJ, 573, L13
Marinacci F. et al., 2018, MNRAS, 480, 5113
Marinacci F., Vogelsberger M., Mocz P., Pakmor R., 2015, MNRAS, 453, 3999
McCarthy I. G., Schaye J., Bird S., Le Brun A. M. C., 2017, MNRAS, 465, 2936
McCourt M., Parrish I. J., Sharma P., Quataert E., 2011, MNRAS, 413, 1295
McDonald M. et al., 2013, ApJ, 774, 23
McDonald M. et al., 2017, ApJ, 843, 28
Naiman J. P. et al., 2018, MNRAS, 477, 1206
Nelson D. et al., 2018, MNRAS, 475, 624
Nelson D., Genel S., Pillepich A., Vogelsberger M., Springel V., Hernquist L., 2016, MNRAS, 460, 2881
Parrish I. J., Quataert E., 2008, ApJ, 677, L9
Parrish I. J., Stone J. M., 2007, ApJ, 664, 135
Parrish I. J., Quataert E., Sharma P., 2010, ApJ, 712, L194
Peterson J. R., Kahn S. M., Paerels F. B. S., Kaastra J. S., Tamura T., Bleeker J. A. M., Ferrigno C., Jernigan J. G., 2003, ApJ, 590, 207
Pfrommer C., 2013, ApJ, 779, 10
Pillepich A. et al., 2018a, MNRAS, 473, 4077
Pillepich A. et al., 2018b, MNRAS, 475, 648
Planck CollaborationXIII, 2016, A&A, 594, A13
Pratt G. W. et al., 2010, A&A, 511, A85
Quataert E., 2008, ApJ, 673, 758
Rasera Y., Chandran B., 2008, ApJ, 685, 105
Rasia E. et al., 2015, ApJ, 813, L17
Roberg-Clark G. T., Drake J. F., Reynolds C. S., Swisdak M., 2016, ApJ, 830, L9
Ruszkowski M., Oh S. P., 2010, ApJ, 713, 1332
Ruszkowski M., Yang H.-Y. K., Reynolds C. S., 2017, ApJ, 844, 13
Sharma P., Chandran B. D. G., Quataert E., Parrish I. J., 2009, ApJ, 699, 348
Sharma P., Parrish I. J., Quataert E., 2010, ApJ, 720, 652
Sijacki D., Vogelsberger M., Genel S., Springel V., Torrey P., Snyder G. F., Nelson D., Hernquist L., 2015, MNRAS, 452, 575
Soker N., 2003, MNRAS, 342, 463
Spitzer L., 1962, Physics of Fully Ionized Gases
Springel V. et al., 2018, MNRAS, 475, 676
Springel V., Hernquist L., 2003, MNRAS, 339, 289
Torrey P., Vogelsberger M., Genel S., Sijacki D., Springel V., Hernquist L., 2014, MNRAS, 438, 1985
Vazza F., Brunetti G., Brüggen M., Bonafede A., 2018, MNRAS, 474, 1672
Vikhlinin A., Markevitch M., Murray S. S., Jones C., Forman W., Van Speybroeck L., 2005, ApJ, 628, 655
Vogelsberger M. et al., 2014a, MNRAS, 444, 1518
Vogelsberger M. et al., 2014b, Nature, 509, 177
Vogelsberger M. et al., 2018, MNRAS, 474, 2073
Vogelsberger M., Genel S., Sijacki D., Torrey P., Springel V., Hernquist L., 2013, MNRAS, 436, 3031
Voigt L. M., Fabian A. C., 2004, MNRAS, 347, 1130
Voit G. M., 2011, ApJ, 740, 28
Voit G. M., Donahue M., 2015, ApJ, 799, L1
Voit G. M., Donahue M., Bryan G. L., McDonald M., 2015, Nature, 519, 203
Voit G. M., Meece G., Li Y., O'Shea B. W., Bryan G. L., Donahue M., 2017, ApJ, 845, 80
Weinberger R. et al., 2017, MNRAS, 465, 3291
Weinberger R. et al., 2018, MNRAS, 479, 4056
Yang H.-Y. K., Reynolds C. S., 2016, ApJ, 818, 181
Zakamska N. L., Narayan R., 2003, ApJ, 582, 162
ZuHone J. A., Markevitch M., Ruszkowski M., Lee D., 2013, ApJ, 762, 69

APPENDIX: TABLE OF CLUSTER PROPERTIES

Table A1. Table presenting the mass, radius, virial temperature, and central conduction time-scale at $z = 0$ for the clusters used in this work.

Cluster	M_{500} ($M_\odot$)	r_{500} (Mpc)	$k_B T_{500}$ (keV)	τ_{cond} (Myr)
A-01	1.02×10^{14}	0.73	1.86	13.8
A-02	5.82×10^{14}	1.30	5.95	27.8
A-03	6.58×10^{14}	1.35	6.45	45.1
A-04	5.01×10^{14}	1.23	5.38	39.1
A-05	5.43×10^{14}	1.27	5.68	106.6
A-06	4.36×10^{14}	1.18	4.90	57.8
A-07	4.20×10^{14}	1.16	4.78	13.3
A-08	6.25×10^{14}	1.33	6.24	41.7
A-09	7.14×10^{14}	1.39	6.81	131.0
A-10	6.44×10^{14}	1.34	6.36	12.5
A-11	8.75×10^{14}	1.49	7.80	153.5
A-12	2.72×10^{15}	2.17	16.62	29.1

This paper has been typeset from a TEX/LATEX file prepared by the author.